The Estimation of the Spatial Response Function

Second for a Remote Sensing Pencil Beam Scatterometer

Three Applied to the RapidScat Scatterometer

Samuel G. Bury

A thesis submitted to the faculty of
Brigham Young University
in partial fulfillment of the requirements for the degree of

Master of Science

David G. Long, Chair
Daniel Smalley
Cammy Peterson

Department of Electrical and Computer Engineering

Brigham Young University

ABSTRACT

The Estimation of the Spatial Response Function
Second for a Remote Sensing Pencil Beam Scatterometer
Three Applied to the RapidScat Scatterometer

Samuel G. Bury
Department of Electrical and Computer Engineering, BYU
Master of Science

This is my abstract.

ACKNOWLEDGMENTS

Thank you to everybody.

TABLE OF CONTENTS

LIST OF TABLES

LIST OF FIGURES

CHAPTER 1.   INTRODUCTION

A scatterometer is a space-borne radar instrument which measures the normalized radar cross-section (σ°) of the Earth's surface. RapidScat is the most recent scatterometer operating in Ku-band. As such, it is hoped that RapidScat data will contribute to the extensive existing scatterometer data set after being cross-calibrated and after the antenna pointing is validated. This chapter provides background on the history of scatterometers. The measurement geometry of a conically scanning pencil beam scatterometer, particularly RapidScat, is discussed. The mathematical formulation of radar backscatter measurements is given in order to introduce the spatial response funciton (SRF). A history of how the SRF has been previously used in scatterometer research is given. I give my thesis statement regarding the use of the SRF in validating the RapidScat antenna pointing. Finally, I explain the organization for the rest of this thesis.

1.1   Scatterometer History

The first scatterometer was designed to observe the correlation between σ° and ocean winds. This was NASA's Seasat-A Satellite Scatterometer System (SASS) launched in June 1978. SASS was operational until October 1978 [2], and provided the first scatterometer data from which global radar measurements of ocean wind were produced [3]. The Earth Remote Sensing (ERS) Scatterometer (ESCAT) was the next operational space-borne scatterometer, launched by the European Space Agency (ESA) aboard ERS-1 in July 1991 and ERS-2 in April 1995. These instruments were in use until March 2000 and September 2011, respectively [4]. In September 1996, shortly the launch of ERS-2, the NASA Scatterometer (NSCAT) was launched to continue the Ku-band ocean vector wind mission begun by SASS [2]. NSCAT was operational from September 1996 to June 1997. SASS, ESCAT, and NSCAT all used fixed fan-beam antennas [2].

The Seawinds instrument on QuikSCAT, referred to as QuikSCAT, was the first wind scatterometer to employ a rotating pencil beam antenna design. QuikSCAT was fully operational

from July 1999 to November 2009 and continues in a post-operational mission to the present day. QuikSCAT successfully produced a ten-year global scatterometer data set spanning 1999-2009 [5]. The scientific community has benefitted greatly from having a long data set that is consistent in quality and coverage.

Another scatterometer which has proved useful in scatterometer climate studies is the Advanced Scatterometer (ASCAT) launched on the European Organisation for the Exploitation of Meterological Satellites (EUMETSAT) MetOp-A satellite in October 2006 and on MetOp-B in September 2012 [6]. Unlike QuikSCAT and NSCAT which operate at Ku-band, ASCAT operates at C-band like its European predecessor ESCAT. ASCAT also uses a fan-beam antenna design and continues to provide useful radar data. The Oceansat-2 Scatterometer (OSCAT) was the second pencil-beam scatterometer to be launched. OSCAT was launched on board the Oceansat-2 satellite in September 2009 by the India Space Research Organization (ISRO) to replicate the success of the QuikSCAT. OSCAT failed in April 2014 [7] [8].

Scatterometers were originally designed to measure ocean vector winds. However, since the first scatterometer was launched, the data provided by each of these sensors has played a part in various other climate studies, including: soil moisture mapping [9], rainforest vegetation density [10], hurricane tracking [11], oil spill clean-up [12], and iceberg tracking [13]. These research areas follow naturally from using $\sigma°$ as a measure of surface roughness and scattering characteristics like what is done in measuring ocean winds. Over time, algorithms have been developed to produce images from scatterometer data and to enhance the resolution of said images [14].

RapidScat is the most recent NASA scatterometer. It originally served as the engineering model for QuikSCAT and was launched as an independent sensor in September 2014. Due to the success of the QuikSCAT mission, RapidScat was designed to resemble the QuikSCAT system as closely as possible given the differences in platform and a table comparing the operating parameters of RapidScat and QuikSCAT is shown in Fig. 1.1. RapidScat is mounted on the International Space Station (ISS) which follows an equatorial orbit, unlike any preceeding scatterometer platform. The ISS also introduces a lower altitude and many attitude variations into the RapidScat measurement geometry. While RapidScat has the same primary scientific objectives as QuikSCAT - to measure ocean vector winds - other interesting qualities of the Earth including diurnal vegetation cycles in

the Amazon have already been observed with RapidScat σ° data [15]. These studies are uniquely suited to RapidScat because it has an equatorial orbit.

Parameter	RapidScat	QuikSCAT	Unit
Orbital attitude	435	800	km
Antenna size	0.75	1	m
3dB beamwidth – 1 way - elevation	2.4, 2.2	1.6, 1.4	degree
3 dB beamwidth – 1 way - azimuth	2.1	1.8, 1.7	degree
Antenna rotation rate	18	18	rpm
Operating frequency	13.4	13.4	GHz
Chirp rate	250	250	kHz/ms
Pulse width	1.0	1.5	ms
PRI	6.0	5.4	ms
Peak radiated power	80	80	W
Incidence angle, 2 beams	49, 56	46, 54	degree
Look angle, 2 beams	45, 50.5	40, 46	degree
Ground-range resolution	0.79, 0.73	0.55, 0.49	km
Azimuth resolution	15.5, 17.3	24.5, 26.0	km
Slant range	600, 678	1095, 1242	km
Ground swath	900, 1100	1410,1800	km
Data window length	1.4	1.8	ms
NE sigma0	-32.8, -31.5	-31.2, -32.2	dB

Figure 1.1: A table reporting the operating parameters for RapidScat compared with the corresponding parameters for QuikSCAT [1].

1.2 Measurement Geometry for RapidScat

This thesis is primarily concerned with RapidScat which is a conically scanning pencil-beam scatterometer. The measurement geometry of this particular class of scatterometer is explained in this section.

RapidScat uses a 0.75-meter-diameter rotating dish to scan the Earth's surface with an elliptically shaped beam footprint. The surface is scanned in a swath directly nadir to the radar as the ISS orbits. An illustration of this measurement system is shown in Fig. 1.2 below. RapidScat uses both a vertically polarized (V-pol) beam and a horizantally polarized (H-pol) beam. The H-pol beam is the inner beam and the V-pol beam is the outer beam.
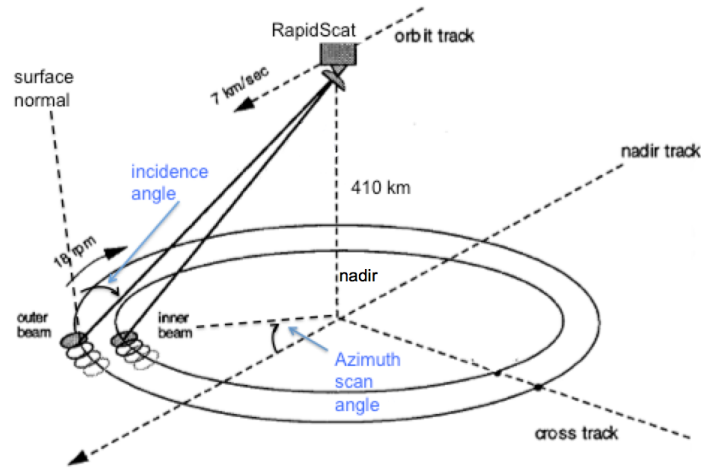
Figure 1.2: An illustration of the measurement geometry of a conically scanning pencil beam scatterometer. [1].

As the antenna rotates about the nadir vector, the radar alternates between transmit mode and receive mode. So, at a certain time, a pulse is transmitted and, at a certain time later, the power which is backscattered by the Earth's surface is received. The antenna illuminates the Earth at both of these times but the illuminated area on the surface, the footprint, is shifted in azimuth between the time of transmission and reception. The product of these two one-way antenna patterns yields a two-way antenna pattern that is illustrated in Fig. 1.3. The darker area where the two ellipses, antenna patterns, overlap is the two-way antenna pattern. The transmit and receive patterns are shifted relative to each other because of the rotation of the antenna during time of flight of the pulse.This two-way antenna pattern dominates the spatial response function which is described in greater detail in the next section. The specifics of the shifted one-way patterns is addressed later in this thesis.

1.3 The Spatial Response Function

The spatial response function (SRF) is the two-way antenna pattern for a scatterometer combined with the processign and filtering done in the radar system electronics. The SRF is also referred to as the impulse response function (IRF), the measurement response function (MRF), or the measurement point-spread function. The physical meaning of the SRF as a weighting function for σ° [14] is discussed in this section.
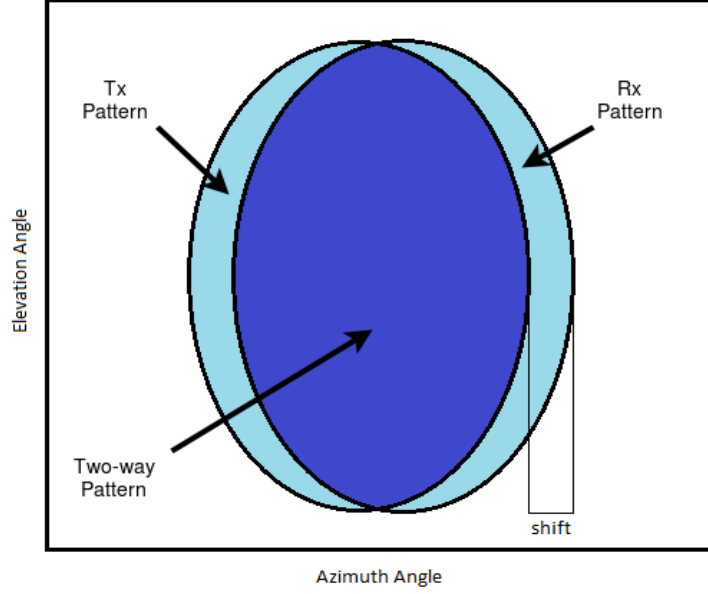
Figure 1.3: An illustration of the shift in the antenna pattern with the change in the antenna position between transmit-time and receive-time. The darker area corresponds to the area of the main lobe of the two-way antenna pattern.

Here, the SRF is derived from the radar equation to show that it is a weighting function. The power received by a radar is

$$P_r = P_b + P_n \tag{1.1}$$

where P_b is the backscattered power and P_n in the noise power from interfering microwave sources and the radar system electronics. The monostatic radar equation for backscattered power, P_b, is given as

$$P_b = \frac{P_t \lambda^2}{(4\pi)^3} \int_A \frac{G^2(\vec{v}) \sigma^\circ(\vec{v})}{r^4(\vec{v})} d\vec{v}, \tag{1.2}$$

where P_t is transmit power, λ is wavelength, r is slant range, A is the area illuminated by the footprint, G is the one-way gain pattern, σ° is the backscatter coefficient, and $\vec{v}$ represents the location of element $d\vec{v}$ within A over a well-defined coordinate system. The radar detects a spatially weighted average of the surface backscatter coefficient which varies over the illuminated area. The signal-only weighted spatial average of σ° is $\bar{\sigma}^\circ$ as seen,

$$\bar{\sigma}^\circ = \frac{P_b}{P_t} \frac{(4\pi)^3}{\lambda^2} \bigg/ \int_A \frac{G^2(\vec{v})}{r^4(\vec{v})} d\vec{v}, \tag{1.3}$$

which can be rewritten as

$$\bar{\sigma}^\circ = \frac{P_b}{X},$$

(1.4)

where X is the X-factor commonly used in scatterometer data post-processing,

$$X = \frac{P_t \lambda^2}{(4\pi)^3} \int_A \frac{G^2(\vec{v})}{r^4(\vec{v})} d\vec{v}.$$

(1.5)

Ashcraft and Long [14], derived an expression for the SRF as follows by substituting Eqs. 1.2 and 1.5 into 1.4 :

$$\bar{\sigma}^\circ = \int_A \frac{G^2(\vec{v})\sigma^\circ(\vec{v})}{r^4(\vec{v})} d\vec{v} \Big/ \int_A \frac{G^2(\vec{v})}{r^4(\vec{v})} d\vec{v},$$

(1.6)

A weighting function, h', for σ° can be defined as

$$h'(\vec{v}) = \frac{G^2(\vec{v})}{r^4(\vec{v})}.$$

(1.7)

This implies that the value of the SRF varies with changing gain and slant range over the footprint defined in $\vec{v}$. So, a different SRF would need to be defined for every measurement due to varying observation geometry. Instead, it is beneficial to remove the dependence of the SRF on slant range in order to eventually estimate a nominal SRF. Appendix A explains the justification for using a constant slant range per measurement so $r^4(\vec{v})$ can be written as simply r^4.

The function $h'(\vec{v})$ is normalized to integrate to 1 by dividing h' by h_0 where

$$h_0 = \int_A \frac{G^2(\vec{v})}{r^4} d\vec{v}.$$

(1.8)

This process yields a normalized weighting function, h, which is the SRF,

$$h(\vec{v}) = \frac{h'(\vec{v})}{h_0},$$

(1.9)

such that

$$\int_A h(\vec{v})d\vec{v} = 1.$$

(1.10)

The spatial variable A is the area on the Earth's surface which is illuminated by the main lobe of the two-way antenna pattern seen in Fig. 1.3. The SRF is integrated over this area because it is dominated by the two-way antenna pattern.

The relationship between the SRF, h, and the observed backscatter is seen by the inner-product

$$\bar{\sigma}^\circ = \int_A h(\vec{v})\sigma^\circ(\vec{v})d\vec{v}, \tag{1.11}$$

where h is the SRF.

The backscattered power is estimated by

$$\hat{P}_b = P_r - \hat{P}_n, \tag{1.12}$$

where $\hat{P}_n$ is an estimate of the noise power. Using $\hat{P}_b$ and Eq. (1.4), an estimate of $\bar{\sigma}^\circ$ is

$$z = \frac{\hat{P}_b}{X} = \bar{\sigma}^\circ + e, \tag{1.13}$$

where e is the noise-like error in the estimation process. The value z is recorded as the radar measurement of the surface σ°. Substituting Eq. (1.11) into Eq. (1.13), z is expressed in terms of the SRF, σ°, and estimation error

$$z = \int_A h(\vec{v})\sigma^\circ(\vec{v})d\vec{v} + e. \tag{1.14}$$

1.4   The Spatial Response Function in Scatterometer Research

Accurate knowledge of the SRF is required to apply high-resolution image reconstruction algorithms to backscatter measurements [14] as well as to calibrate scatterometers for wind retrieval [3]. Early and Long [16], and Williams and Long [17] describe the use of the aperture function, or SRF, in sampling scatterometer data for use in image reconstruction. σ° data is "aperture-filtered" because the SRF is used as a low-pass filter over the σ° of the surface. Thus, knowledge of the shape, size, and frequency response of the SRF is critical for implementing these image processing algorithms.

In the case of QuikSCAT, the known antenna pattern permits the SRF for each measurement to be calculated and tabulated as a function of the antenna rotation angle, and orbit position [14]. Joshua Bradley developed a method of estimating the SRF for Oceansat-2 (OSCAT) using an island target and a rank-reduced least squares approach [18]. Bradley's method proved effective for estimating the OSCAT SRF and [18] shows the improvements in OSCAT image reconstruction using the estimated SRF.

1.5 Thesis Statement

The previously developed methods for estimating the scatterometer SRF required stability in the attitude of the radar platform. Despite the success of Bradley's estimation algorithm in the case of OSCAT, RapidScat has proven to be more difficult due to large variations over time in attitude geometry. RapidScat's irregular geometry suggests that a different approach needs to be applied. Changing the coordinate system over which the SRF is estimated from a ground-based coordinate system to an angle-based coordinate system accounts for the variations in geometry. This yields an estimate of the SRF which is more robust to changes in attitude. This thesis presents a method of estimating the SRF for RapidScat which employs an angle-based coordinate system. The usefulness of the SRF in validating the pointing of RapidScat is also demonstrated in this thesis.

The contributions that my work adds to the field of scatterometry are:

- An alternate method for estimating the SRF of a pencil-beam scatterometer which is more robust to changes in platform attitude

- A demonstration of how an estimate of the SRF can be used to validate the antenna pointing of a pencil-beam scatterometer

1.6 Thesis Organization

This thesis is organized in the following order. Chapter 2 provides the mathematical structure for performing the rank-reduced least squares procedure to estimate the SRF. Chapter 3 describes the dimensions of the radiation pattern for a generic dish antenna. Chapter 4 lays out the

methods of estimating the SRF using an angle-based coordinate system. Chapter 5 shows the way in which the SRF is used to validate the antenna pointing for RapidScat. Chapter 6 derives a method of approximating the one-way antenna pattern from the estimated SRF. Chapter 7 summarizes the results of this thesis and draws comparisons from previous work done on estimating the SRF. Chapter 8 concludes with a description of the contributions this thesis adds to the scatterometer research community and suggests areas of future work on this topic.

CHAPTER 2.   SPATIAL RESPONSE FUNCTION ESTIMATION MODEL

Joshua Bradley developed a procedure for estimating the OSCAT SRF where he employs the technique of sampling the SRF with carefully selected island targets [18]. Due to the fact that an island is much brighter than the dark ocean background, a small, isolated island is an approximation of a delta function. So, the radar measurements taken over an island can be viewed as samples of the SRF. These measurements are compiled into a matrix which is inverted to estiamte the SRF. This same method can be used to estimate the RapidScat SRF. The mathematical details of the process are given in this chapter.

This chapter shows the way in which σ° measurements are compiled into a matrix in order to invert the radar equation and solve for the SRF. The inversion process using a singular value decomposition (SVD) is described. The mathematical development contained in this chapter closely follows a similar development in [18].

2.1   Estimation Model

Following the derivation of the SRF and the expression of Eq. (1.14), the m-th measurement, z_m, received by a scatterometer can be modeled as

$$z_m = \int_A h(\vec{v})\sigma^\circ(\gamma_m, \vec{x}_m, \vec{v})d\vec{v} + e_m, \tag{2.1}$$

where the normalized radar backscatter, σ°, is a function of γ_m, which encapsulates the parameters of the observation geometry including azimuth angle and incidence angle, and $\vec{x}_m$ which is the orbital location of the radar. Here, the SRF, h, is assumed to be independent of γ_m and $\vec{x}_m$. The e_m term is the noise-like error in the estimate of the signal only power for the m-th measurement. The bound of integration, A, is the area illuminated by the two-way antenna pattern. Both h and σ° are defined over the coordinate system $\vec{v}$. Historically, $\vec{v}$ has been defined in x and y on the Earth's

surface [18]. An alternative approach is presented in this thesis which defines $\vec{v}$ in azimuth and elevation angle independent of the surface. This is explained in greater detail in Chapter 4 of this thesis. For the sake of notational simplicity, the derivation in this chapter uses $\vec{v}$.

The inner product of Eq. (2.1) can be discretized as a sum over a sufficiently fine resolution sample grid for the SRF,

$$z_m \approx \sum_{k=1}^{K} h(\vec{v}_k)\sigma^{\circ}(\gamma_m, \vec{x}_m, \vec{v}_k)\Delta v + e_m, \tag{2.2}$$

where K is the number of grid elements and Δv is the constant area of each grid element (defined in the coordinate system of $\vec{v}$). This expression can be expressed as a vector inner product,

$$z_m \approx \mathbf{S}_m^T \mathbf{h} + e_m, \tag{2.3}$$

where,

$$\mathbf{S}_m = \begin{bmatrix} \sigma^{\circ}(\gamma_m, \vec{x}_m, \vec{v}_1) \\ \sigma^{\circ}(\gamma_m, \vec{x}_m, \vec{v}_2) \\ \vdots \\ \sigma^{\circ}(\gamma_m, \vec{x}_m, \vec{v}_K) \end{bmatrix} \Delta v, \tag{2.4}$$

$$\mathbf{h} = \begin{bmatrix} h(\vec{v}_1) \\ h(\vec{v}_2) \\ \vdots \\ h(\vec{v}_K) \end{bmatrix}. \tag{2.5}$$

Collecting M measurements over the K element grid yields a $M \times K$ matrix Q where each row represents the σ° for each grid element for the m-th measurement. Many measurements need to be used in order to sample each element, $d\vec{v}$, of the coordinate system, $\vec{v}$.

$$\mathbf{z} = \begin{bmatrix} z1 \\ z2 \\ \vdots \\ z_M \end{bmatrix} \approx \begin{bmatrix} \mathbf{S}_1^T \\ \mathbf{S}_2^T \\ \vdots \\ \mathbf{S}_M^T \end{bmatrix} \mathbf{h} + \begin{bmatrix} e_1 \\ e_2 \\ \vdots \\ e_M \end{bmatrix} = Q\mathbf{h} + \mathbf{e}, \tag{2.6}$$

The **h** is the discretized SRF. We can calculate a least-squares estimate of the SRF, $\hat{\mathbf{h}}_{LS}$, by performing a pseudo-inverse on Q

$$\hat{\mathbf{h}}_{LS} = Q^{\dagger}\mathbf{z}, \tag{2.7}$$

where $Q^{\dagger}$ is the Moore-Penrose pseudo-inverse $Q^{\dagger} = (Q^H Q)^{-1}Q^H$. In order to improve the conditioning of Q to yield a closer approximation of the inverse, a rank-reduced approximation using the SVD of Q is done before the pseudo-inverse so that

$$\mathbf{z} = U\Sigma V^H \mathbf{h} + \mathbf{e}, \tag{2.8}$$

$$= \tilde{Q}\mathbf{h} + \mathbf{e}, \tag{2.9}$$

where U is a unitary $M \times M$ matrix, V is a unitary $K \times K$ matrix which has as its columns the eigenvectors of Q, and Σ is a $M \times K$ matrix with the singular values of Q down the main diagonal. The matrix $\tilde{Q}$ can be decomposed as

$$\tilde{Q} = \begin{bmatrix} U_1 & U_2 \end{bmatrix} \begin{bmatrix} \Sigma_1 & 0 \\ 0 & \Sigma_2 \end{bmatrix} \begin{bmatrix} V_1^H \\ V_2^H \end{bmatrix} = U_1\Sigma_1 V_1^H + U_2\Sigma_2 V_2^H. \tag{2.10}$$

The matrices U_1, Σ_1, and V_1 are the portions of U, Σ, and V which correspond to the largest singular values of Q which represent the signal. U_2, Σ_2, and V_2 correspond to all of the smaller singular values which represent noise. Q is approximated by setting the small singular values to zero, which reduces the rank. We are then left with

$$\tilde{Q} \approx U_1\Sigma_1 V_1^H, \tag{2.11}$$

$$\hat{\mathbf{h}}_{SVD} = \tilde{Q}^{\dagger}\mathbf{z} = V_1\Sigma_1^{-1}U_1^H\mathbf{z}. \tag{2.12}$$

The precise number of singular values to use in the estimate is a tuning parameter for the SRF estimate that is discussed more in Appendix B.

2.2 Summary

This chapter describes the way in which samples of the SRF are be used to invert the radar equation to solve for the SRF. Each measurement is modeled as a vector inner product and many measurements are combined to sample the whole grid over which the SRF is defined. Performing an SVD on the matrix of measurements and eliminating noise terms yields a useful estimate of the SRF.

CHAPTER 3.   ESTIMATION OF THE SPATIAL RESPONSE FUNCTION

There are several steps required to estimate the RapidScat SRF using on-orbit data. These steps for RapidScat are generally the same as the steps for estimating the OSCAT SRF [18]. There are several differences which have been made to the process in order to accomodate the highly variable observation geometery for RapidScat. The most crucial of these differences are manifest in the coordinate system used to create the landmap and over which the SRF is sampled. Bradley used a landmap in kilometers on the ground (ground-based). A new coordinate system for the landmap, in beam azimuth and elevation angles (angle-based), is useful for RapidScat because of geometric variations from measurement to measurement.

This chapter describes each of the steps in the process of estimating the SRF. First, the methods used to collect measurements for the estimation process are explained. Creating the landmap to sample the SRF is discussed. The differences which were made in the case of the RapidScat SRF estimation are explained and the differences between the two sampling coordinate systems are presented. Then, the procedure for removing the ocean σ° bias from the land contribution to σ° is reviewed. Finally, the rank-reduced least squares estimation of the SRF described in depth in Chapter 2 is briefly addressed as the concluding step in the estimation process.

3.1   Selecting Measurements

In order for Eq. (2.12 to yield a good estimate of the SRF, as many measurements as possible should be combined into the Q matrix. A colleciton of σ° measurements over Rarotonga Island, capital of the Cook Islands are used in the estimation of the RapidScat SRF. Rarotonga is one of the island identified by Joshua Bradley to qualify as an approximate delta function. A few key statistics about Rarotonga are given in the tabel below. The following high resoulion QuikSCAT image shows Rarotonga in the center with other islands several hundred kilometers away.

14

Table 3.1: Rarotonga Island Information

Latitude	-159.776°
Longitude	-21.229°
Max. Width	11 km
Area	67.39 km²
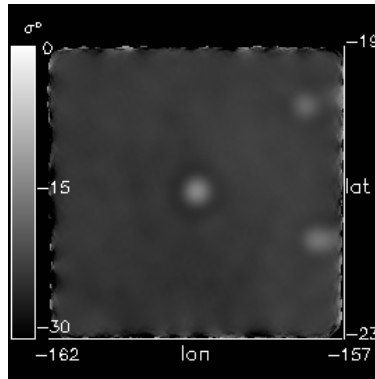
Figure 3.1: A high resolution QuikSCAT egg backscatter image of the region around Rarotonga. Rarotonga is the bright dot in the center of the image.

The measurements which fall into this region are found by searching all of the RapidScat Level-1B (L1B) data by date. Almost a year of data is used, specifically Julian Day (JD) 276 of year 2014 to JD 220 of year 2015. This date range covers the time for which RapidScat was in a high singal-to-noise ratio (SNR) state. Other SNR states are avoided in order to simplify the estimation proces by maintaining the same level of quality in the data.

During the finding process, the sigma0_qual_flag, frame_err_status, and the frame_qual_flag were checked to ensure that onl the highest fidelity measurements were being used [19]. If any of these flags were set, the measurement or the frame were thrown out. This is a change that needed to be made for the RapidScat estimation because there were so few erroneaous measurements with OSCAT that the estimation was not significantly affected. RapidScat has various states which make the flags all the more important. For example, the are times when RapidScat is turned off in order to avoid radiating the ISS.

Another change that I made to simplify the measurement finding process was eliminate the use of SIR images. Setting a simple threshold on latitude and longitude to determine if a

measurement fell within the specified region rather than converting to pixel values in a SIR image streamlined the process.

For all measurements that are good quality and are located within the appropriate region, key information - regarding the geometry, σ°, and so forth - is written to a setup file for easy access in the next processing steps.

3.2 Building the Sample Landmap

Assuming the σ° across the island is a constant for any given measurement, the vector $\mathbf{S}_m$ from Eq. (2.3) can be written as

$$\mathbf{S}_m = [landmap]^T \sigma_L^\circ \Delta v, \tag{3.1}$$

where $landmap$ is a vector of 1's and 0's indicating which grid elements within the SRF correspond to land, σ_L° is the land component of the reported σ°, and Δv is the area of each grid element in the landmap. As mentioned previously, the cluster of 1's representing the island is small compared to the overall grid for the SRF. Therefore, each $\mathbf{S}_m$ corresponds to one sample of the SRF. A discussion of how to approximate σ_L° is given in the next section. The methods for building the landmap are described in this section. This section also explains the choice in coordinate system over which the land map, and therefore the SRF, is defined.

3.2.1 Review of Method for OSCAT

When Bradley developed the original version of this algorithm for OSCAT, the coordinate system $\vec{v}$ was in (x,y) displacement in kilometers on the ground. The origin of his coordinate system for the SRF estimate was the position at which the boresight vector of the antenna was incident on the ground. Bradley fixed the orientation of the island in his estimation, with the vertical axis being North-South and the horizontal axis being East-West, and used the reported antenna rotation angle to rotate the SRF into the same orientation as the island in the search grid. The figure below illustrates this coordinate system.
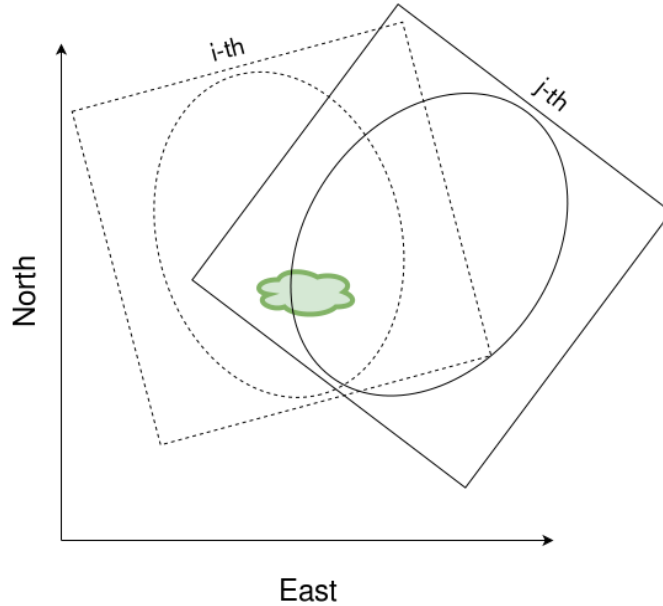
Figure 3.2: An illustration of the coordinate system used to build the *landmap* in the OSCAT SRF estimation, for the i-th and the j-th measurements. The SRF is rotated in to the North-East coordinate system and then the *landmap* is constructed from gridding the rotated frames.

This method extensively used SIR images to define distances from the island in pixels, the location of the SRF relative to the island, and the search grid over which the $\mathbf{S}_m$ vectors are compiled. The SIR images also provided a useful standard of pixel size on which to define the size of the footprint on the ground. The *landmap* was constructed for each measurement by selecting a certain number of pixels from the center of the location of the SRF. The SRF estimate was eventually computed to be in kilometers on the ground. This worked for OSCAT because the geometry (attitude, altitude, slant range) was fairly stable. This means that the shape and size of the OSCAT beam footprint (i.e., the SRF) on the ground were nearly constant.

3.2.2 The Method for RapidScat

RapidScat has a lot of variability in attitude and altitude so the beam footprint dimensions on the ground cannot be assumed to be constant like that of OSCAT. This is problematic because, the estimation procedure uses the size of the beam on the ground in kilometers to define distances and to decide if a measurement is an ocean measurement or a land measurement. These challenges motivated the use of a different coordinate system.

17

The huge variations in slant range and attitude can be accomodates for the most part by computing the SRF estimate using a fixed boresight angle and a randomly placed and oriented island. The angle bearing from the spacecraft for the measurement boresight becomes relevant only to locate the island in the search grid. Then the island location can be specified as an azimuth and elevation angle coordinate relative to the boresight of the antenna. The *landmap* is made by converting the angle coordinates of each grid element into latitude and longitude and determining if the (lat,lon) is land or not. The following figure illustrates how the island is located relative to the boresight.
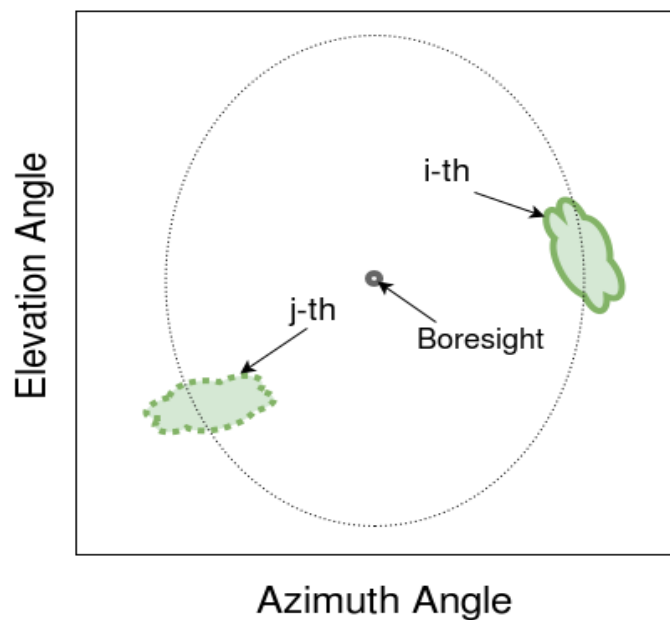
Figure 3.3: An illustration of the coordinate system used to build the *landmap* in the RapidScat SRF estimation, for the i-th and the j-th measurements. The island is located in azimuth and elevation angle relative to the boresight. The *landmap* is made by determining which pixels in the frame are land.

This new coordinate system is implemented using the BYU X-factor computation routines. First, the latitude and longitude for each measurement is converted into an azimuth and elevation angle from the nadir vector of the spacecraft. Then the known location in latitude and longitude of the island is used to compute the same angles for the island relative to the spacecraft. Subtracting the boresight angles from the island angles sets the boresight at the origin of an angle-based coordinate system in beam azimuth and elevation from the antenna boresight. The island, with

the calculated angles, is then located within an the angle grid centered on the antenna boresight at transmit time (the latitude and longitude reported in the RapidScat L1B data is the latitiude and longitude of the boresight at transmit time).

Once the island location is specified in the angle-based coordinate system, each pixel in the grid is tested for land. This is done by converting the azimuth and elevation angles of each grid element to latitude and longitude and then tested for land using the world land map. If a grid element is land, it is marked with a 1, and a 0 otherwise. This grid, essentially a local landmap, is then normalized to sum to 1 and is written column by column into the *landmap* of Eq. (3.1). The normalization occurs because the integration of power received at the antenna is the reported σ° which is being multiplied by the local land map. Thus, the integration of the land map must equal 1. The normalization is also useful to make every measurement including a piece of the island equal in weight for the overall estimation process and to remove any dependence on the dimensions of the footprint on the ground.

3.3 Removing the Ocean Bias from σ°

Measurements over a small island target inevitably include contributions to σ° from the land, σ_L°, and from the ocean, σ_O°. The combination of σ_L° and σ_O° can be understood by

$$\sigma^\circ = \sigma_L^\circ + \sigma_O^\circ \tag{3.2}$$

Since, the approximation of the island as a delta function requires that all of the backscattered power is due to σ_L°, σ_O° must be negligible. Bradley used a spatially varying quadratic fit on σ_O° to estimate the ocean contribution to σ° over land.

In the method developed for OSCAT, the pixels that were outside a certain pixel width were considered ocean and the contribution of the ocean, σ_O°, was estimated and subtracted out of σ° as seen by

$$\sigma_L^\circ = \sigma^\circ - \hat{\sigma}^\circ{}_O, \tag{3.3}$$

where $\hat{\sigma}^{\circ}{}_O$ is the estimated σ°_O. The estimation and subtraction is done for every pass because σ°_O can be assumed constant for one pass but not multiple due to weather conditions. This process yields σ°_L to be used in Eq. (3.1) to compute $\mathbf{S}_m$.

In the case of RapidScat, the same method of estimating σ°_O is used. However, the land measurements and ocean measurements are determined by an angle distance away from the boresight rather than a number of pixels in a SIR image grid.

3.4 Solving for the SRF

After unbiasing each measurement and building the corresponding *landmap*, each $\mathbf{S}_m$ represents the contribution of one measurement to the SRF estimate. The M, $\mathbf{S}_m$ vectors are compiled as rows to create the Q matrix seen in Eq. (2.6). This is the matrix which is inverted using the singular-value decomposition to solve for the SRF.

3.5 Conclusion

This process yields a good estimate of the RapidScat SRF defined in beam azimuth and elevation angle. The primary difference made to the SRF estimation process for RapidScat is the change in coordinate system. This new coordinate system is an improvement for RapidScat because the SRF geometry variations are all accounted for in changing the way that the *landmap* is built. The angle grid is able to include changes in geometry like slant range for example, because as the slant range changes, the range of latitude and longitude covered by a single grid element adjusts appropriately. In other words, the value of Δv from Eq. 3.1 is fixed in the angle-based coordinate system and it is only treated as a fixed value in the ground-based coordinate system when in reality the footprint of the two-way antenna pattern is different for every measurement. The angle-based SRF estimate is also very helpful because of the clarity intuition regarding how the antenna pointing might influence the SRF. If there were biases in the antenna pointing, they would be seen in a constant shift in the center of the SRF.

REFERENCES

[1] "RapidScat." [Online]. Available: https://winds.jpl.nasa.gov/missions/RapidScat/

[2] "Instrument description: Spaceborne scatterometers." [Online]. Available: https://nsidc.org/data/docs/daac/scatterometer_instrument.gd.html

[3] D. G. Long, "High resolution wind retrieval from SeaWinds," *Geoscience and Remote Sensing Symposium*, vol. 2, pp. 751–753, 2002.

[4] "What is ERS?" [Online]. Available: https://earth.esa.int/web/guest/missions/esa-operational-eo-missions/ers

[5] "QuikSCAT." [Online]. Available: https://winds.jpl.nasa.gov/missions/quikscat/#mission

[6] "Ascat." [Online]. Available: http://www.remss.com/missions/ascat

[7] "OceanSat-2." [Online]. Available: https://directory.eoportal.org/web/eoportal/satellite-missions/o/oceansat-2

[8] "OceanSat-2." [Online]. Available: https://manati.star.nesdis.noaa.gov/products/OSCAT.php

[9] W. Wagner, J. Noll, M. Borgeaud, and H. Rott, "Monitoring soil moisture over the Canadian prairies with the ERS scatterometer," *IEEE Transactions on Geoscience and Remote Sensing*, vol. 37, no. 1, pp. 206–216, 1999.

[10] D. G. Long and P. J. Hardin, "Vegetation studies of the Amazon basin using enhanced resolution Seasat scatterometer data," *IEEE Transactions on Geoscience and Remote Sensing*, vol. 32, no. 2, pp. 449–460, 1994.

[11] B. A. Williams and D. G. Long, "Estimation of hurricane winds from SeaWinds at ultrahigh resolution," *IEEE Transactions on Geoscience and Remote Sensing*, vol. 46, no. 10, pp. 2924–2935, 2008.

[12] R. D. Lindsley and D. G. Long, "Mapping surface oil extent from the Deepwater Horizon oil spill using ASCAT backscatter," *IEEE Transactions on Geoscience and Remote Sensing*, vol. 50, no. 7, pp. 2534–2541, 2012.

[13] J. Ballantyne and D. G. Long, "A multidecadal study of the number of Antarctic icebergs using scatterometer data," *Geoscience and Remote Sensing Symposium*, vol. 5, pp. 3029–3031, 2002.

[14] I. S. Ashcraft and D. G. Long, "The spatial response function of SeaWinds backscatter measurements," *Proceedings of SPIE*, vol. 5151, pp. 609–618, 2003.

[15] A. C. Paget, D. G. Long, and N. M. Madsen, "Rapidscat diurnal cycles over land," *IEEE Transactions on Geoscience and Remote Sensing*, vol. 54, no. 6, pp. 3336–3344, 2016.

[16] D. S. Early and D. G. Long, "Image reconstruction and enhanced resolution imaging from irregular samples," *IEEE Transactions on Geoscience and Remote Sensing*, vol. 39, no. 2, pp. 291–302, 2001.

[17] B. A. Williams and D. G. Long, "Reconstruction from aperture-filtered samples with application to scatterometer image reconstruction," *IEEE Transactions on Geoscience and Remote Sensing*, vol. 49, no. 5, pp. 1663–1676, 2011.

[18] J. P. Bradley and D. G. Long, "Estimation of the OSCAT spatial response function using island targets," *IEEE Transactions on Geoscience and Remote Sensing*, vol. 52, no. 6, pp. 1924–1934, 2014.

[19] "QuikSCAT Science Data Product User's Manual," 2006. [Online]. Available: ftp://podaac.jpl.nasa.gov/allData/quikscat/L2A/v2/docs/QSUG_v3.pdf

APPENDIX A.   SLANT RANGE DEPENDENCE OF THE SRF

For any given measurement, the slant range from the radar to the surface varies over the illuminated two-way antenna pattern. The expression given by Eq. (1.7) shows that the SRF which is defined over $\vec{v}$ is a funtion of the gain G and the slant range r. Both G and r are functions of $\vec{v}$ which includes the observation geometery for r. Since the geometry is different for every measurement, the SRF would need to be recomputed for every measurement. This makes the estimation process described in Chapter 2 cumbersome and impractical. To solve for a nominal SRF rather than an SRF for every measurement, the dependence of r on $\vec{v}$ can be removed.

This appendix presents a reasonable approximation for the slant range. The approximation is verified with parameters from RapidScat.

A.1   Approximation of Slant Range

Consider defining the slant range at each point within the footprint as

$$r = r_0 + \Delta r, \tag{A.1}$$

$$= r_0 \left(1 + \frac{\Delta r}{r_0} \right), \tag{A.2}$$

where r_0 is the slant range to the center of the footprint on the ground and Δr is the difference between r_0 and the slant range to any other point within the footprint. Since r_0 is much greater than Δr the ratio $\Delta r/r_0$ is very small and $r \approx r_0$.

A.2   The Case of RapidScat

In order to verify this slant range approximation for RapidScat, the parameters contained in Fig. (1.1) can be used to calculate the approximate variations in slant range. Only the variations in slant range in the elevation dimension of the beam are significant because the slant range across

the azimuth dimension is almost constant. Using the law of cosines, the maximum slant range and the minimum slant range in the elevation dimension can be computed. The computed values are found in the table below.

Table A.1: RapidScat Slant Range Variations

Nominal Slant Range (r_0)	600 km
Max. Slant Range	609.54 km
Min. Slant Range	590.57 km
Max. Δr	9.54 km
Ratio $\frac{\Delta r}{r_0}$	0.0159
Nominal r^4	1.2960×10^{11} km^4
Max. r^4	1.3804×10^{11} km^4
Max. Percent Error	6.12%

The values in the table above show that it is a reasonable approximation to ignore the variations in slant range over the coordinate system $\vec{v}$ in the case of RapidScat.